ACS APPLIED NANO MATERIALS

Article

Cite This: ACS Appl. Nano Mater. 2019, 2, 6334−6342

www.acsanm.org

Oxygen-Evolution Catalysts Based on Iron-Mediated Nickel Metal−Organic Frameworks

Zixia Wan,[†] Dandan Yang,[†] Judan Chen,[†] Jianniao Tian,[†] Tayirjan Taylor Isimjan,[*,‡] and Xiulin Yang[*,†]

[†]Guangxi Key Laboratory of Low Carbon Energy Materials, School of Chemistry and Pharmaceutical Sciences, Guangxi Normal University, Guilin 541004, People's Republic of China

[‡]Saudi Arabia Basic Industries Corporation (SABIC) at King Abdullah University of Science and Technology (KAUST), Thuwal 23955-6900, Saudi Arabia

Supporting Information

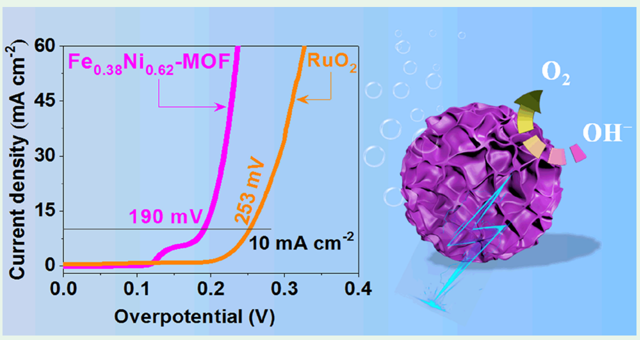

ABSTRACT: Metal−organic frameworks (MOFs) based oxygen-evolution reaction (OER) catalyst is an emerging class of highly porous materials that have become increasingly attractive to develop a highly active and stable OER catalyst for overall water splitting. However, it suffers from poor conductivity and inadequate active sites. Herein, we have developed a series of hierarchical Fe-mediated Ni-based metal−organic frameworks (Fe_xNi_{1-x}-MOF) by an adjustable hydrolysis strategy, where the Ni-MOF is used as a template that is decorated with NiOOH active sites. Although Ni-MOF is dissociated during the ion exchange process, the structural integrity is kept for Fe_xNi_{1-x}-MOF as confirmed by the electron micrographs. Moreover, the optimized $Fe_{0.38}Ni_{0.62}$-MOF catalyst not only exhibits a remarkable OER catalytic performance with a low overpotential of 190 mV at 10 mA cm^{-2} but also shows a small Tafel slope of 58.3 mV dec^{-1} and stability. The excellent OER electrocatalytic activity can be attributed to the unique 3D flower-like structure decorated with NiOOH active sites induced by Fe^{3+} species. This novel methodology expands a new way for the construction of highly efficient alkaline catalytic materials.

KEYWORDS: *oxygen-evolution reaction, Fe-mediated Ni-organic framework, hierarchical structure, hydrolysis, coupling effect*

■ INTRODUCTION

With the constant depletion of fossil fuels and the increasingly severe environmental problems, environmentally friendly energy storage and sustainable energy technologies have gradually become research hotspots.[1,2] The transition-metal-based organic−inorganic hybrid materials including carbon-confined or sulfides@graphene hybrid catalyst have been widely explored for energy storage as well as conversion applications.[3,4] Water splitting in electrochemistry to produce H_2 and O_2 is an effective tactic to solve future energy and environmental problems.[5,6] Electrocatalytic water splitting utilizes oxygen-evolution reaction (OER) as the anode.[7] However, the OER catalytic efficiency is minimal by sluggish kinetics in electrocatalytic oxidation.[8] This is associated with critical electrochemical processes in many energy conversion devices. Therefore, the anode of water splitting to obtain O_2 is of great significance and challenge.[9,10] Up to now, the scarcity and high costs of IrO_2 or RuO_2 have limited their widespread application, although these materials present the most effective OER activity and reduce high overpotential.[11,12] Hence, it is an extreme challenge to develop high-efficiency, inexpensive, earth-abundant, and stable non-noble-metal-based OER catalysts. Interestingly, transition-metal oxides/hydroxides such as nickel iron oxides, nickel hydroxide, and nickel−iron bimetallic hydroxide have been studied extensively for their promising OER properties.[13,14] Nevertheless, the insufficient electrical conductivity and lack of active sites of these materials are widely recognized as the main challenges to improve their OER.[15]

Metal−organic frameworks (MOFs), a promising coordination complex, has a large surface area and controllable 1D, 2D, and 3D porous structure, which presents great potential for the noble-metal-free OER catalysts.[16,17] Moreover, MOF can be easily functionalized by other metal ions to add a new functionality through methathesis,[18−24] such as Zhu and co-workers' successfully synthesized 2D Ni-MOF@Fe-MOF nanosheets that demonstrated a high electrocatalytic performance toward OER. The outstanding performance was ascribed to the 2D nanosheet morphology as well as the synergistic effect between Ni active centers and Fe species.[25] Meanwhile,

Received: July 14, 2019
Accepted: September 9, 2019
Published: September 9, 2019

Scheme 1. Schematic Illustration of the Synthesis Process for the Fe_xNi_{1-x}-MOF (FMN-*x*h)

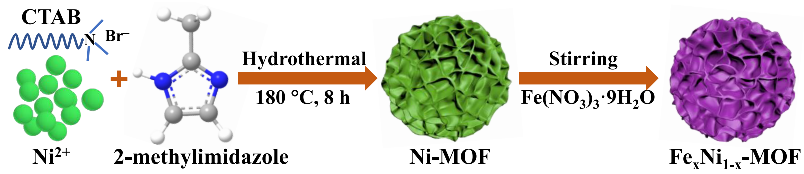

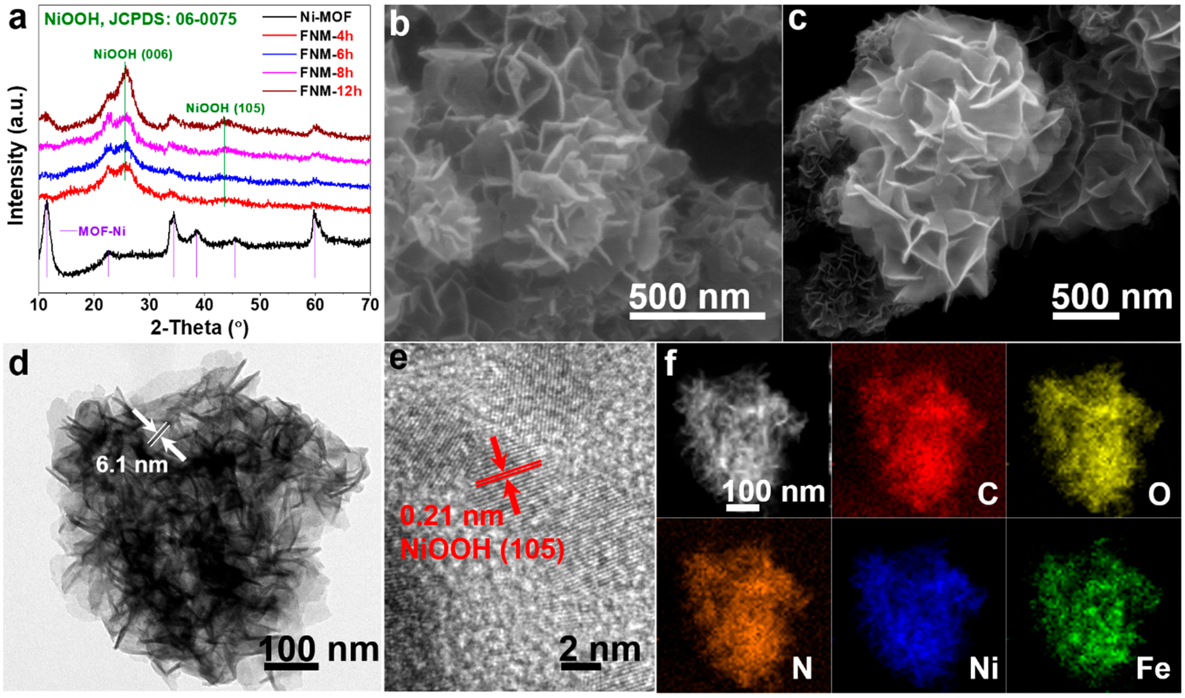

Figure 1. (a) XRD patterns of Fe modulated Ni-MOF with different reaction times. SEM images of (b) Ni-MOF and (c) $Fe_{0.38}Ni_{0.62}$-MOF. (d) TEM and (e) HRTEM images of $Fe_{0.38}Ni_{0.62}$-MOF. (f) HAADF-STEM image of $Fe_{0.38}Ni_{0.62}$-MOF and the corresponding elemental mappings of C, O, N, Ni, and Fe.

Chen and co-workers attested to a series of Hofmann MOFs with a malty metal ions center and altered OER activity through the synergistic effects between different metal ions.[26,27] While these exploratory studies demonstrated a high potential of mixed metal MOF for OER application, the utilization of MOFs in electrocatalysis was still limited due to poor conductivity, small pore size, and embedded active metal centers by organic ligands.[28] Besides, the fabrication of highly active transition-metal MOF-based OER catalysts with the accelerated kinetics of four-electron ($4e^-$) processes remains a significant challenge.[29] More importantly, insufficient knowledge of the catalytic mechanisms further limits the optimal design of high-efficiency and low-cost transition-metal MOF-based catalysts for water splitting.

In this work, we developed a facile route to fabricate a novel series of hierarchical porous Fe−Ni-based methylimidazole MOFs (Fe_xNi_{1-x}-MOF). The optimized $Fe_{0.38}Ni_{0.62}$-MOF showed a remarkably low overpotential (190 mV at a current density of 10 mA cm^{-2}) and small Tafel slope (58.3 mV dec^{-1}) in 1.0 M KOH, which is among the best reported so far. Furthermore, the crystal structure, microstructure, surface functional group, thermal stability, and porosity of the materials are carefully characterized. The catalytic mechanism analysis found that the contents of Fe/Ni and their different chemical states played a crucial role in the OER activity, and the effect of Fe species was also discussed in detail.

■ EXPERIMENTAL SECTION

Synthesis of Ni-MOF. All chemical reagents are used as analytical grade without further purification. In a facile synthesis, 0.58 g of $Ni(NO_3)_2·6H_2O$ and 0.05 g of CTAB are uniformly dispersed in 30 mL of methanol and followed by slow injection of 0.66 g of 2-methylimidazole in 30 mL of methanol under continuous stirring within 30 min. The resulted dark green solution was transformed into a Teflon-lined stainless autoclave (90 mL) and kept at 180 °C for 8 h. After cooling to room temperature, the mixture was centrifuged, washed with abundant methanol three times, and then vacuum-dried at 60 °C for 12 h to prepare the product of Ni-MOF.

Synthesis of Iron-Modulated Ni-MOF Composite. A dispersion of 50 mg of Ni-MOF and $Fe(NO_3)_3·9H_2O$ in 5 mL of water was stirred for 1.0 h, and then another 5 mL of 0.234 M NaOH and 0.068 M Na_2CO_3 were added dropwise. The resulting suspension was stirred for different times (3, 5, 7, and 11 h) and then centrifuged. The resulted solids are nominated as Fe_xNi_{1-x}-MOF or abbreviated as FNM-*y*h (*y* = 4, 6, 8, and 12) according to the total soaking times.

Preparation of Catalytic Electrode. Prior to the preparation of the catalytic electrode, the carbon cloths (CC, 1 cm × 3 cm) were cleaned ultrasonically in 0.5 M HCl, ethanol, and water, respectively, and then dried in air.

The fresh FNM-*y*h composite prepared above was ultrasonically dispersed into 2 mL of ethanol, and 1 mL of this solution was pipetted onto both sides of the carbon cloth (1 cm × 3 cm). After drying, 120 μL of 0.5 wt % Nafion was dropped on the surface of the catalytic materials and then dried naturally to prepare a series of catalytic electrodes. The catalyst loading is measured to be ~5.0 mg cm^{-2} by a precision balance.

DOI: 10.1021/acsanm.9b01330
ACS Appl. Nano Mater. 2019, 2, 6334−6342

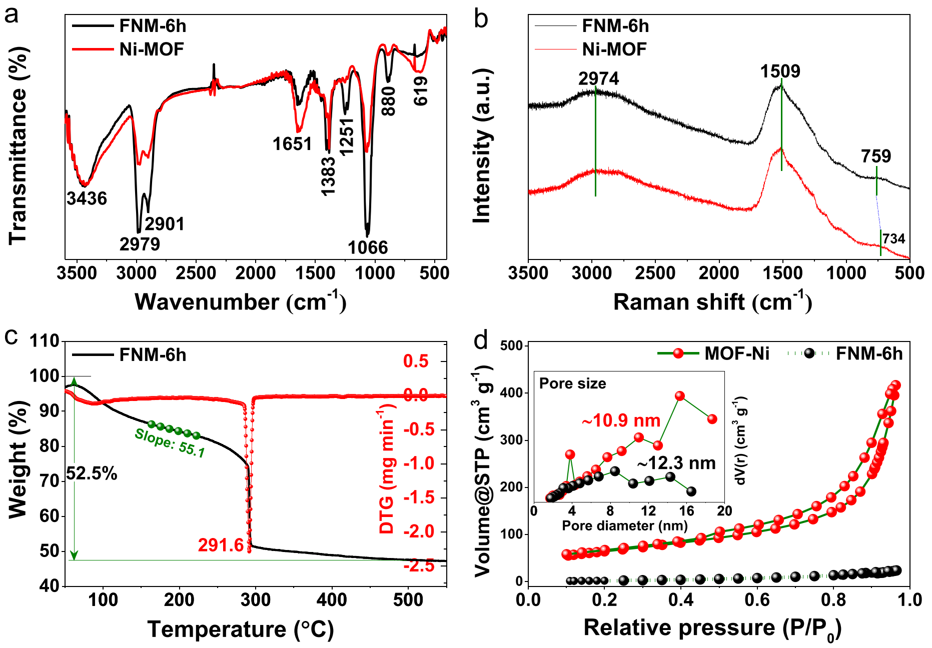

Figure 2. (a) FTIR and (b) Raman spectrum of $Fe_{0.38}Ni_{0.62}$-MOF and Ni-MOF. (c) Thermal gravimetric (TG) analysis and derivative thermal gravimetry (DTG) curves of $Fe_{0.38}Ni_{0.62}$-MOF in O_2 atmosphere with a rising temperature rate of 2.5 °C min^{-1}. (d) N_2 adsorption−desorption isotherms with the pore size distribution curves by the BJH method (inset) of Ni-MOF and $Fe_{0.38}Ni_{0.62}$-MOF.

Electrochemical Measurements. All electrochemical measurements were executed in a standard three-electrode system operated by a VMP3 electrochemical workstation. Catalysts loaded CC was used as the working electrode, a saturated calomel electrode (SCE) as the reference, and a graphite sheet as the counter electrode. Polarization curves were acquired using linear sweep voltammetry (LSV) at a scan rate of 0.2 mV s^{-1} in 1.0 M KOH solution. The frequency range of electrochemical impedance spectroscopy (EIS) is from 200 kHz to 0.1 Hz. The chronopotentiometry has studied the long-term stability of catalysts. In the current crossed zero (1.040 V), all potentials measured were calibrated to the RHE to obtain the thermodynamic potential by the average CV curves of the two potentials in H_2-saturated 1.0 M KOH (Supporting Information Figure S1). The result is lower than $E(\text{RHE}) = E(\text{SCE}) + 0.241 + 0.059\text{pH} = E(\text{SCE}) + (1.049\ \text{V})$ (pH = 13.7). All curves reported were *iR* compensated, and all of the electrochemical tests were carried out at room temperature (25 ± 1 °C). The CV tests on catalysts are measured at varied scan rates in 1.0 M KOH solution to determine the electrochemical double-layer capacitance (C_{dl}) between the non-Faradaic potential windows. The turnover frequency (TOF) was calculated by the following formula:

$$\text{TOF} = \frac{JA}{4Fn} \tag{1}$$

where J is the current density and A corresponds to the geometric surface area of the electrode. F is the Faraday constant (96,485 C mol^{-1}), and n is the moles of all metal atoms loaded on the CC. It is worth noting that all of the metal atoms were assumed as active species.[30,31]

RESULTS AND DISCUSSION

Synthetic Strategy Analysis. The series Fe_xNi_{1-x}-MOF materials were prepared by a simple two-step process including hydrothermal synthesis of Ni-MOF and subsequent soaking in $Fe(NO_3)_3$ solution (Scheme 1). The pristine Ni-MOF was first fabricated by hydrothermal treatment of 2-methylimidazole, $Ni(NO_3)_2$, and CTAB in methanol solution at 180 °C for 8 h, in which the CTAB surfactant regulates the orientation of Ni species and 2-methylimidazole in coordination to Ni-MOF.[32] Thereafter, the Ni-MOF was dispersed in an aqueous solution of $Fe(NO_3)_3$, the Fe ions can be immersed where the Ni species were partially substituted by Fe species while keeping the structural integrity of the original MOF. Thereby a series of Fe_xNi_{1-x}-MOF (FNM-*y*h, *y* = 4, 6, 8 or 12) composites were obtained after optimizing the pH value and reaction time. The elemental analyzer results revealed that the N contents of the composites decreased with the prolonged soaking times suggesting 2-methylimidazole leaching from the Ni-MOF (Table S1). Besides, the Ni/Fe in different Fe_xNi_{1-x}-MOF was measured by inductively coupled plasma spectrometer (ICP, Table S2). The composite of FNM-6h can be expressed as $Fe_{0.38}Ni_{0.62}$-MOF as discussed below.

Structures and Characterization Analysis. The crystal structure changes of different materials are investigated by X-ray diffraction (XRD) patterns. As shown in Figure 1a, the XRD patterns are consistent with the previously reported Ni-MOF.[32] After soaking in $Fe(NO_3)_3$ solution for different times, the diffraction peaks of Ni-MOF became weaker and two additional diffraction peaks, which represent (006) and (105) of NiOOH (JCPDS No. 06-0075), appeared.[33,34] No diffraction peak of the known Fe species such as FeO or Fe_2O_3 was detected; this could be an indirect indication of Fe replacing Ni in the MOF structure and leaching out Ni to form NiOOH in the solution.

The morphological of Ni-MOF and the optimal $Fe_{0.38}Ni_{0.62}$-MOF were further explored by scanning electron microscopy (SEM) and transmission electron microscopy (TEM). The SEM images show that both Ni-MOF and $Fe_{0.38}Ni_{0.62}$-MOF have a flower-like structure composed of two-dimensional nanosheets (Figure 1b), and not detectable damage on the MOF morphology was observed after the ion exchange process (Figure 1c). Besides, the SEM images of FNM-*y*h materials obtained in different soaking times are shown in Figure S2 which reveal a flower-like structure. However, the flower-like feature tends to disappear with time.

DOI: 10.1021/acsanm.9b01330
ACS Appl. Nano Mater. 2019, 2, 6334−6342

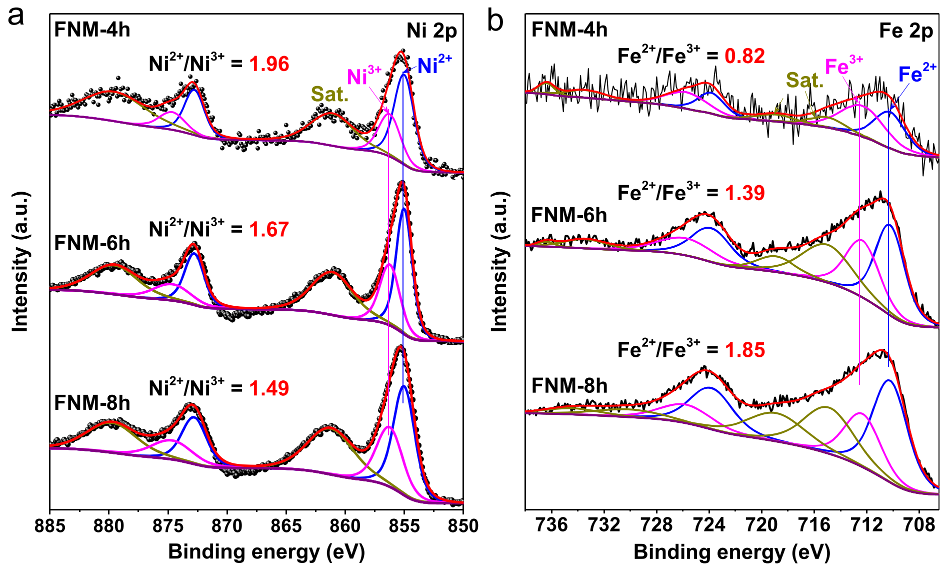

Figure 3. High-resolution XPS spectra of (a) Ni 2p and (b) Fe 2p from FNM-4h ($Fe_{0.32}Ni_{0.68}$-MOF), FNM-6h ($Fe_{0.38}Ni_{0.62}$-MOF), and FNM-8h ($Fe_{0.46}Ni_{0.54}$-MOF), respectively.

The TEM image of $Fe_{0.38}Ni_{0.62}$-MOF shows that the flower-like structure consists of ultrathin nanosheets and possesses an average thickness of about 6.1 nm (Figure 1d). The ultrathin nanosheets not only expose sufficient active sites but also are advantageous to the charge and mass transfer, thereby enhancing the OER catalytic performance. The high-resolution TEM image shows a lattice fringe with a lattice spacing of approximately 0.21 nm (Figure 1e), which matches with the (105) crystal plane of NiOOH.[33] No lattice fringe of Ni-MOF was detected, which indicates that Ni-MOF dissociates during the ion exchange process. The HAADF-STEM and the elemental mapping images of $Fe_{0.38}Ni_{0.62}$-MOF prove the uniformly distribution of C, O, N, Ni, and Fe on the surface of the composite (Figure 1f).

Fourier transform infrared spectroscopy (FTIR) was used to study the surface functional groups and formation of $Fe_{0.38}Ni_{0.62}$-MOF. Ni-MOF and $Fe_{0.38}Ni_{0.62}$-MOF have somewhat similar features except for the peak at 1251 cm^{-1} (Figure 2a) that could belong to the bending vibration of NO_3^-.[35] The peak at 3436 cm^{-1} is assigned to O−H stretching vibration.[36] The doublet at 2979 and 2901 cm^{-1} belong to the stretching of methyl H and aromatic C−H.[37] The three peaks at 1651, 1383, and 1066 cm^{-1} are attributed to the adsorbed H_2O, C═N, and C−N vibration,[38] and the additional two peaks at 880 and 619 cm^{-1} are the characteristic peaks of metal−oxygen and the five-membered aromatic ring, respectively.[37,39] These typical functional group vibration peaks confirm the presence of an MOF bridge-coordinated structure. Moreover, the doublet (2979 and 2901 cm^{-1}) of Ni-MOF is much weaker than that of $Fe_{0.38}Ni_{0.62}$-MOF, indicating some aromatic C−H have been protonated during the Fe and Ni ions exchange process and further suggesting the disintegration of Ni-MOF. Furthermore, the Raman spectrum of Ni-MOF exhibits three distinctive peaks at around 734, 1509, and 2974 cm^{-1}, which are corresponding to the metal−oxygen disordered vibration, C═C stretching mode, and stretching vibrations of C−H unsaturated bonds of Ni-MOF (Figure 2b).[40,41] Interestingly, the Raman shift of the metal−oxygen vibration in $Fe_{0.38}Ni_{0.62}$-MOF was blue-shifted relative to Ni-MOF, indicating that the soaking of the $Fe(NO_3)_3$ solution changes in the metal coordination bond in Ni-MOF.[42]

Thermogravimetric analysis (TGA) was further used to study the mass variation during the pyrolysis of both $Fe_{0.38}Ni_{0.62}$-MOF and Ni-MOF under the oxygen atmosphere (Figure 2c and Figure S3). The mass loss at temperatures below 120 °C is primarily due to the evaporation of adsorbed water.[43] At higher temperatures, as well as a strong exothermic peak of 291.6 or 307.7 °C, it is mainly attributed to the pyrolysis of organic frameworks, oxidation of metal ions, or dehydration of metal hydroxides.[44] It is worth noting that the mass loss rate of $Fe_{0.38}Ni_{0.62}$-MOF is 55.1 mass $°C^{-1}$, which is much higher than 40.3 mass $°C^{-1}$ of Ni-MOF in a similar temperature range. The significant rate loss and the reduced exothermic temperature on $Fe_{0.38}Ni_{0.62}$-MOF once again illustrate the partial damaging of Ni-MOF because of Fe ions exchange. The Brunauer−Emmett−Teller (BET) gas-sorption measurements demonstrate that the Ni-MOF material has a type III isotherm with a distinct hysteresis loop at relative pressures (P/P_0) of 0.43−1.0 (Figure 2d), and the corresponding BET specific surface area is about 229.0 m^2 g^{-1}. However, the relative BET specific surface area of $Fe_{0.38}Ni_{0.62}$-MOF is approximately 11.8 m^2 g^{-1}, further indicating structural collapsing of Ni-MOF. Although the value of BET is somewhat smaller than Ni-MOF, $Fe_{0.38}Ni_{0.62}$-MOF exhibits excellent OER performance. This result indicates that the surface morphology is the critical factor but not the only element to define OER performance where we should also consider the number of active sites that resulted by NiOOH as well as the synergy between Ni and Fe species. In another words, the OER activity of the optimized catalyst is the fruit of the combined effect of the various factors mentioned above. Meanwhile, the average pore size distribution of the $Fe_{0.38}Ni_{0.62}$-MOF is also slightly larger than that of Ni-MOF.

The surface compositions and chemical states of the as-prepared series of Fe_xNi_{1-x}-MOF and Ni-MOF materials are detected by X-ray photoelectron spectroscopy (XPS). The $Fe_{0.38}Ni_{0.62}$-MOF material is composed of the elements of C, O, N, Ni, and Fe (Figure S4a). The high-resolution C 1s spectrum fitted to C−C (284.8 eV) and C−O (286.0 eV) was

DOI: 10.1021/acsanm.9b01330
ACS Appl. Nano Mater. 2019, 2, 6334−6342

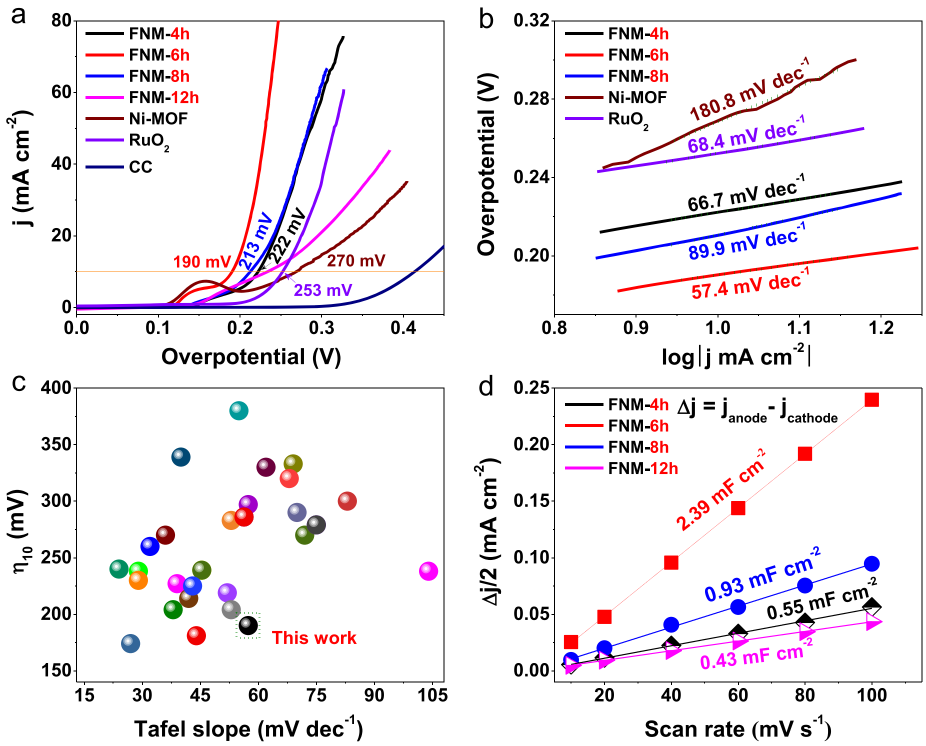

Figure 4. OER catalytic performance of different catalysts in 1.0 M KOH. (a) LSV curves with a scan rate of 0.2 mV s^{-1}. (b) Tafel slopes calculated from LSV curves. (c) Summarized overpotentials of the recently reported catalysts at 10 mA cm^{-2} and the corresponding Tafel slopes (Table S2). (d) Summarized double-layer capacitance (C_{dl}) of different catalysts.

used as the calibration standard (Figure S4b).[45] The high-resolution O 1s spectrum is shown in Figure S4c, where the O species at 530.3 and 531.1 eV are corresponding to the metal−oxygen (M−O) and M−OH bonds, respectively.[46] The O species at 532.8 eV is typical for the adsorbed H_2O.[47] In addition, it can be observed that the ratio of Ni^{2+}/Ni^{3+} in the high-resolution Ni 2p region is 4.92 (Figure S4d), and the high-resolution N 1s spectrum only contains pyridinic-N (398.5 eV) and pyrrolic-N (399.9 eV) in the pristine Ni-MOF (Figure S4e) as reported in literature.[48] The peak fittings of Ni 2p from Fe_xNi_{1-x}-MOF are revealed in Figure 3a where the peaks at 855.0, and 872.8 eV belong to Ni^{2+} species, those at 856.2 and 874.7 eV are attributed to Ni^{3+} species, and the third pair of peaks are assigned as satellite peaks.[49,50]

It is worth noting that the Ni^{2+}/Ni^{3+} ratios of Fe_xNi_{1-x}-MOF decrease when the soaking time increases and the values are significantly lower than that of Ni-MOF (4.92), suggesting a great deal of dissociation of Ni-MOF during the soaking step. In addition, Fe species are also detected on series of Fe_xNi_{1-x}-MOF materials (Figure 3b). Four pairs of peaks are fitted in the high-resolution XPS spectra of Fe 2p, in which the binding energies at 710.2 and 723.8 eV are assigned to Fe^{2+} species and those at 712.3 and 725.8 eV originate from Fe^{3+} species, while the other two pairs of peaks belong to satellite.[51] Contrary to the Ni, the Fe^{2+}/Fe^{3+} ratio increased with the increasing $Fe(NO_3)_3$ soaking times. Some Fe^{3+} ions are reduced to Fe^{2+} species ($Fe^{3+} + e^- \rightarrow Fe^{2+}$, $\varphi^\ominus = +0.77$ V), while Ni^{2+} species are oxidized to Ni^{3+} species ($NiOOH + H_2O + e^- \rightarrow Ni(OH)_2 + OH^-$, $\varphi^\ominus = +0.49$ V) with the increasing soaking times pointing to the formation of Fe_xNi_{1-x}-MOF with different redox states of Fe/Ni species.[52]

OER Catalytic Performance. The OER performance of a series of Fe_xNi_{1-x}-MOF, Ni-MOF, RuO_2/CC, and CC catalysts are evaluated in a 1.0 M KOH solution, and all LSV polarization curves are processed by *iR* compensation and RHE correction. The electrochemical impedance spectroscopy (EIS) results of all catalysts are shown in Figure S5, where the optimal $Fe_{0.38}Ni_{0.62}$-MOF exhibits much lower charge-transfer impedance (R_{ct} = 2.40 Ω) than those of $Fe_{0.32}Ni_{0.68}$-MOF (R_{ct} = 2.45 Ω), $Fe_{0.46}Ni_{0.54}$-MOF (R_{ct} = 4.56 Ω), and RuO_2 (R_{ct} = 4.60 Ω). Prior to testing the LSV curves, the CV curves were measured up to five cycles until the curves have a reasonable overlap. Since the Fe_xNi_{1-x}-MOF and Ni-MOF catalysts have a pair of distinctive Ni^{2+}/Ni^{3+} redox peaks in the overpotential range of 0.1−0.2 V ($Ni(OH)_2 + OH^- \leftrightarrow NiOOH + H_2O + e^-$),[34,53] a low scan rate (0.2 mV s^{-1}) was used to reduce the effect of the scan rate. As shown in Figure 4a, the Fe_xNi_{1-x}-MOF catalyst only requires 190 mV overpotential to deliver current density of 10 mA cm^{-2}, which is far lower than all control catalysts including the RuO_2/CC (253 mV). In addition, the $Fe_{0.38}Ni_{0.62}$-MOF also shows the smallest Tafel slope of 57.4 mV dec^{-1}, suggesting fast reaction kinetics and a superior OER activity (Figure 4b).[19] Notably, the OER activity of $Fe_{0.38}Ni_{0.62}$-MOF is further highlighted by comparing to the high-performance MOF-based catalyst as well as other OER catalysts reported in alkaline media (Figure 4c, Table S3).[16,18,54,55]

In general, a favorable OER catalytic activity relates with a large electrochemical active surface area (EASA) which is proportional to C_{dl}. The EASAs of the catalysts were calculated according to the following equation:

$$\mathrm{EASA} = \frac{C_{dl}}{C_s} \tag{2}$$

where the C_s is the specific capacitance in an alkaline electrolyte and C_{dl} is obtained from the cyclic voltammetry

DOI: 10.1021/acsanm.9b01330
ACS Appl. Nano Mater. 2019, 2, 6334−6342

(CV) curves within the non-Faradaic region at different scan rates (10, 20, 40, 60, 80, and 100 mV s^{-1}) (Figure S6). The C_{dl} value equals the slope of the linear relationship between the scan rate and current density. As shown in Figure 4d, the experimentally optimized $Fe_{0.38}Ni_{0.62}$-MOF catalyst possesses the highest C_{dl} of 2.39 mF cm^{-2}, and it is ca. 4.35- and 2.57-fold higher than those of $Fe_{0.32}Ni_{0.68}$-MOF and $Fe_{0.46}Ni_{0.54}$-MOF. Besides the EASA, the TOF value also reflects the intrinsic OER activity. As shown in Figure S7, $Fe_{0.38}Ni_{0.62}$-MOF displays a TOF value as high as 3.65 s^{-1} at 250 mV, which is higher than those of $Fe_{0.32}Ni_{0.68}$-MOF (1.39 s^{-1}) and $Fe_{0.46}Ni_{0.54}$-MOF (0.77 s^{-1}). Notably, these catalysts exhibit similar TOF trends when different overpotentials are used as a reference, implying that the active site of $Fe_{0.38}Ni_{0.62}$-MOF has robust catalytic activity.

To investigate the potential industrial application, we explored the overall water splitting in a two-electrode configuration, in which $Fe_{0.38}Ni_{0.62}$-MOF/CC was used as the anode oxygen-generating catalyst and the commercial Pt/C-modified CC was selected as the cathode hydrogen-producing catalyst in1.0 M KOH electrolyte (Figure 5a).

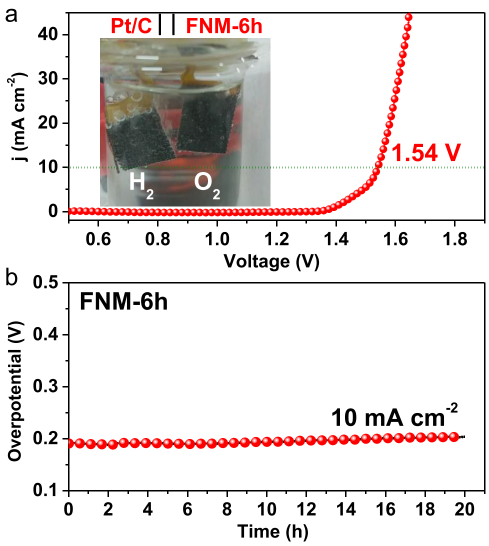

Figure 5. (a) Overall water splitting of $Fe_{0.38}Ni_{0.62}$-MOF and commercial Pt/C on CC surface as anode and cathode electrocatalysts in two-electrode system. (b) Long-term stability test of $Fe_{0.38}Ni_{0.62}$-MOF/CC catalyst continuously operated at 10 mA cm^{-2} for 20 h.

The steady-state polarization curves of the coupled $Fe_{0.38}Ni_{0.62}$-MOF$^{(+)}$//Pt/C$^{(-)}$ on CC requires only a cell voltage of 1.53 V to reach a current density of 10 mA cm^{-2}, superior to most of the previously reported two-electrode catalytic systems.[52,56−58] In addition, the long-term stability of the $Fe_{0.38}Ni_{0.62}$-MOF/CC catalyst was tested at a constant current of 10 mA cm^{-2} in the three-electrode system (Figure 5b), and the catalyst showed an outstanding stability within 20 h of testing. Since the Ni and 2-methylimidazole coordinate MOF was destroyed during the soaking process, there are no apparent changes on the SEM morphology of the $Fe_{0.38}Ni_{0.62}$-MOF (Figures S8 and S9). On another hand, we observed a drastic change on the morphology of Ni-MOF/CC. Electrochemical stability studies showed that the overpotential of the control catalyst increased slowly in a 1.0 M KOH solution at a constant current of 10 mA cm^{-2} for 20 h (Figure S10). At the same time, the SEM images showed that the morphology of MOF-Ni catalyst changed greatly before and after the OER reaction, indicating the dissociation of Ni-MOF structures (Figure S11). From this phenomenon, one can conclude that although Ni-MOF is destroyed during the soaking, the MOF-based scaffold of $Fe_{0.38}Ni_{0.62}$-MOF keeps its structural integrity during the OER test. Notably, the ratio between the different valence states of the Ni and Fe species in the $Fe_{0.38}Ni_{0.62}$-MOF/CC were altered after 20 hours of stability testing due to the intrinsic chemical instability of Ni and Fe species,[59] shedding of partial catalyst, and the chemical corrosion (Figure S12).

The OER mechanism of the Ni-based catalytic materials has been studied in detail, and three intermediate-state catalytic steps are widely accepted,[53,60] described as follows.

$$NiOOH + OH^- \leftrightarrow NiO(OH)_2 + e^- \tag{3}$$

$$NiO(OH)_2 + 2OH^- \rightarrow NiOO_2 + 2H_2O + 2e^- \tag{4}$$

$$NiOO_2 + OH^- \rightarrow NiOOH + O_2 + e^- \tag{5}$$

overall:

$$4OH^- \rightarrow O_2 + 2H_2O + 4e^- \tag{6}$$

where step 5 is the rate-determining step of the catalytic process where the active NiOOH promotes the OH^- oxidation; moreover, a high-valence Fe impurity with strong electron acceptability induces the formation of the high-valence Ni species (NiOOH), thereby accelerating the OER process.[61−64] In the case of MOF-based OER catalyst, the high surface area 3D flower-like MOF structure not only exposes more active sites but also promotes the gas release from the catalyst surface.[65,66] However, the MOF structure collapses with the formation of NiOOH; therefore, there is a diligent balance between NiOOH content and structural integrity of the MOF support to have optimal OER performance. The optimal results were achieved after 6 h of $Fe(NO_3)_3$ soaking.

CONCLUSIONS

In summary, a novel and high-performance $Fe_{0.38}Ni_{0.62}$-MOF catalyst was prepared using Ni-MOF as the porous template. This method is feasible and straightforward; meanwhile, no calcining is required. The catalytic test and characterization results indicate that it is essential to keep the structural integrity of the MOF while increasing the NiOOH content to achieve high performance. The optimized $Fe_{0.38}Ni_{0.62}$-MOF catalyst exhibited the lowest overpotential (190 mV) and the smallest Tafel slope in alkaline media as compared to other Fe_xNi_{1-x}-MOFand Ni-MOF. A two-electrode configuration composed of $Fe_{0.38}Ni_{0.62}$-MOF$^{(+)}$//Pt/C$^{(-)}$ on CC requires only a cell voltage of 1.53 V to reach a current density of 10 mA cm^{-2} and shows high stability, demonstrating a promising application for overall water splitting.

ASSOCIATED CONTENT

Supporting Information

The Supporting Information is available free of charge on the ACS Publications website at DOI: 10.1021/acsanm.9b01330.

Figures S1−S12 and Tables S1−S3 giving more details on characterization of our synthesized materials and their electrocatalytic performance data; additional SEM, XRD, TG, XPS, ICP-AES, and electrocatalytic performance data (PDF)

DOI: 10.1021/acsanm.9b01330
ACS Appl. Nano Mater. 2019, 2, 6334−6342

AUTHOR INFORMATION

Corresponding Authors

*(X.Y.) E-mail: xiulin.yang@kaust.edu.sa.

*(T.T.I.) E-mail: isimjant@sabic.com.

ORCID

Xiulin Yang: 0000-0003-2642-4963

Notes

The authors declare no competing financial interest.

ACKNOWLEDGMENTS

This work has been supported by the National Natural Science Foundation of China (Grant No. 21965005), the Natural Science Foundation of Guangxi Province (Grant Nos. 2018GXNSFAA294077 and 2017GXNSFGA198004), the Project of High-Level Talents of Guangxi (Grant Nos. F-KA18015 and 2018ZD004), and the Innovation Project of Guangxi Graduate Education (Grant Nos. XYCSZ2019056 and YCBZ2019031).

REFERENCES

(1) Zhang, P.; Yu, L.; Lou, X. W. D. Construction of Heterostructured Fe_2O_3-TiO_2 Microdumbbells for Photoelectrochemical Water Oxidation. *Angew. Chem., Int. Ed.* **2018**, *57*, 15076−15080.

(2) Kou, Y.; Liu, J.; Li, Y.; Qu, S.; Ma, C.; Song, Z.; Han, X.; Deng, Y.; Hu, W.; Zhong, C. Electrochemical Oxidation of Chlorine-Doped $Co(OH)_2$ Nanosheet Arrays on Carbon Cloth as a Bifunctional Oxygen Electrode. *ACS Appl. Mater. Interfaces* **2018**, *10*, 796−805.

(3) Du, M.; Song, D.; Huang, A.; Chen, R.; Jin, D.; Rui, K.; Zhang, C.; Zhu, J.; Huang, W. Stereoselectively Assembled Metal-Organic Framework (MOF) Host for Catalytic Synthesis of Carbon Hybrids for Alkaline-Metal-Ion Batteries. *Angew. Chem., Int. Ed.* **2019**, *58*, 5307−5311.

(4) Wang, Q.; Rui, K.; Zhang, C.; Ma, Z.; Xu, J.; Sun, W.; Zhang, W.; Zhu, J.; Huang, W. Interlayer-Expanded Metal Sulfides on Graphene Triggered by a Molecularly Self-Promoting Process for Enhanced Lithium Ion Storage. *ACS Appl. Mater. Interfaces* **2017**, *9*, 40317−40323.

(5) Zhao, Y.; Zhang, J.; Wu, W.; Guo, X.; Xiong, P.; Liu, H.; Wang, G. Cobalt-doped MnO_2 ultrathin nanosheets with abundant oxygen vacancies supported on functionalized carbon nanofibers for efficient oxygen evolution. *Nano Energy* **2018**, *54*, 129−137.

(6) Gupta, S.; Yadav, A.; Bhartiya, S.; Singh, M. K.; Miotello, A.; Sarkar, A.; Patel, N. Co oxide nanostructures for electrocatalytic water-oxidation: effects of dimensionality and related properties. *Nanoscale* **2018**, *10*, 8806−8819.

(7) Babar, P.; Lokhande, A.; Shin, H. H.; Pawar, B.; Gang, M. G.; Pawar, S.; Kim, J. H. Cobalt Iron Hydroxide as a Precious Metal-Free Bifunctional Electrocatalyst for Efficient Overall Water Splitting. *Small* **2018**, *14*, 1702568.

(8) Chen, P.; Zhou, T.; Wang, S.; Zhang, N.; Tong, Y.; Ju, H.; Chu, W.; Wu, C.; Xie, Y. Dynamic Migration of Surface Fluorine-anions on Cobalt-based Materials Realizing Enhanced Oxygen Evolution Catalysis. *Angew. Chem., Int. Ed.* **2018**, *57*, 15471−15475.

(9) Hu, F.; Zhu, S.; Chen, S.; Li, Y.; Ma, L.; Wu, T.; Zhang, Y.; Wang, C.; Liu, C.; Yang, X.; Song, L.; Yang, X.; Xiong, Y. Amorphous Metallic NiFeP: A Conductive Bulk Material Achieving High Activity for Oxygen Evolution Reaction in Both Alkaline and Acidic Media. *Adv. Mater.* **2017**, *29*, 1606570.

(10) Wang, M.; Lin, M.; Li, J.; Huang, L.; Zhuang, Z.; Lin, C.; Zhou, L.; Mai, L. Metal-organic framework derived carbon-confined Ni_2P nanocrystals supported on graphene for efficient oxygen evolution reaction. *Chem. Commun.* **2017**, *53*, 8372−8375.

(11) Jin, Y.; Yue, X.; Du, H.; Wang, K.; Huang, S.; Shen, P. K. One-step growth of nitrogen-decorated iron-nickel sulfide nanosheets for the oxygen evolution reaction. *J. Mater. Chem. A* **2018**, *6*, 5592−5597.

(12) Wang, B.; Tang, C.; Wang, H.-F.; Chen, X.; Cao, R.; Zhang, Q. A Nanosized CoNi Hydroxide@Hydroxysulfide Core-Shell Heterostructure for Enhanced Oxygen Evolution. *Adv. Mater.* **2019**, *31*, 1805658.

(13) Dong, C.; Kou, T.; Gao, H.; Peng, Z.; Zhang, Z. Eutectic-Derived Mesoporous Ni-Fe-O Nanowire Network Catalyzing Oxygen Evolution and Overall Water Splitting. *Adv. Energy Mater.* **2018**, *8*, 1701347.

(14) Zhang, R.; Dubouis, N.; Ben Osman, M.; Yin, W.; Sougrati, M. T.; Corte, D. A. D.; Giaume, D.; Grimaud, A. A Dissolution/Precipitation Equilibrium on the Surface of Iridium-Based Perovskites Controls Their Activity as Oxygen Evolution Reaction Catalysts in Acidic Media. *Angew. Chem., Int. Ed.* **2019**, *58*, 4571−4575.

(15) Wang, W.; Liu, Y.; Li, J.; Luo, J.; Fu, L.; Chen, S. NiFe LDH nanodots anchored on 3D macro/mesoporous carbon as high-performance ORR/OER bifunctional electrocatalyst. *J. Mater. Chem. A* **2018**, *6*, 14299−14306.

(16) Wang, X.; Xiao, H.; Li, A.; Li, Z.; Liu, S.; Zhang, Q.; Gong, Y.; Zheng, L.; Zhu, Y.; Chen, C.; Wang, D.; Peng, Q.; Gu, L.; Han, X.; Li, J.; Li, Y. Constructing NiCo/Fe_3O_4 Heteroparticles within MOF-74 for Efficient Oxygen Evolution Reactions. *J. Am. Chem. Soc.* **2018**, *140*, 15336−15341.

(17) Ma, L.; Zhou, B.; Tang, L.; Guo, J.; Liu, Q.; Zhang, X. Template confined synthesis of NiCo Prussian blue analogue bricks constructed nanowalls as efficient bifunctional electrocatalyst for splitting water. *Electrochim. Acta* **2019**, *318*, 333−341.

(18) Hai, G.; Jia, X.; Zhang, K.; Liu, X.; Wu, Z.; Wang, G. High-performance oxygen evolution catalyst using two-dimensional ultrathin metal-organic frameworks nanosheets. *Nano Energy* **2018**, *44*, 345−352.

(19) Zhao, S.; Wang, Y.; Dong, J.; He, C.-T.; Yin, H.; An, P.; Zhao, K.; Zhang, X.; Gao, C.; Zhang, L.; Lv, J.; Wang, J.; Zhang, J.; Khattak, A. M.; Khan, N. A.; Wei, Z.; Zhang, J.; Liu, S.; Zhao, H.; Tang, Z. Ultrathin metal−organic framework nanosheets for electrocatalytic oxygen evolution. *Nat. Energy* **2016**, *1*, 16184.

(20) Kung, C. W.; Mondloch, J. E.; Wang, T. C.; Bury, W.; Hoffeditz, W.; Klahr, B. M.; Klet, R. C.; Pellin, M. J.; Farha, O. K.; Hupp, J. T. Metal-Organic Framework Thin Films as Platforms for Atomic Layer Deposition of Cobalt Ions To Enable Electrocatalytic Water Oxidation. *ACS Appl. Mater. Interfaces* **2015**, *7*, 28223−28230.

(21) Zhao, X.; Pattengale, B.; Fan, D.; Zou, Z.; Zhao, Y.; Du, J.; Huang, J.; Xu, C. Mixed-Node Metal−Organic Frameworks as Efficient Electrocatalysts for Oxygen Evolution Reaction. *ACS Energy Lett.* **2018**, *3*, 2520−2526.

(22) Cheng, W.; Zhao, X.; Su, H.; Tang, F.; Che, W.; Zhang, H.; Liu, Q. Lattice-strained metal−organic-framework arrays for bifunctional oxygen electrocatalysis. *Nat. Energy* **2019**, *4*, 115−122.

(23) Li, F. L.; Shao, Q.; Huang, X.; Lang, J. P. Nanoscale Trimetallic Metal-Organic Frameworks Enable Efficient Oxygen Evolution Electrocatalysis. *Angew. Chem., Int. Ed.* **2018**, *57*, 1888−1892.

(24) Dou, S.; Dong, C.-L.; Hu, Z.; Huang, Y.-C.; Chen, J.-l.; Tao, L.; Yan, D.; Chen, D.; Shen, S.; Chou, S.; Wang, S. Atomic-Scale CoO_x Species in Metal−Organic Frameworks for Oxygen Evolution Reaction. *Adv. Funct. Mater.* **2017**, *27*, 1702546.

(25) Rui, K.; Zhao, G.; Chen, Y.; Lin, Y.; Zhou, Q.; Chen, J.; Zhu, J.; Sun, W.; Huang, W.; Dou, S. X. Hybrid 2D Dual-Metal-Organic Frameworks for Enhanced Water Oxidation Catalysis. *Adv. Funct. Mater.* **2018**, *28*, 1801554.

(26) Gao, J.; Cong, J.; Wu, Y.; Sun, L.; Yao, J.; Chen, B. Bimetallic Hofmann-Type Metal−Organic Framework Nanoparticles for Efficient Electrocatalysis of Oxygen Evolution Reaction. *ACS Appl. Energy Mater.* **2018**, *1*, 5140−5144.

(27) Zhang, X.; Wu, Y.; Sun, Y.; Liu, Q.; Tang, L.; Guo, J. CoFeP hollow cube as advanced electrocatalyst for water oxidation. *Inorg. Chem. Front.* **2019**, *6*, 604−611.

(28) Xue, Z.; Li, Y.; Zhang, Y.; Geng, W.; Jia, B.; Tang, J.; Bao, S.; Wang, H.-P.; Fan, Y.; Wei, Z.-w.; Zhang, Z.; Ke, Z.; Li, G.; Su, C.-Y. Modulating Electronic Structure of Metal-Organic Framework for

DOI: 10.1021/acsanm.9b01330
ACS Appl. Nano Mater. 2019, 2, 6334−6342

Efficient Electrocatalytic Oxygen Evolution. *Adv. Energy Mater.* **2018**, *8*, 1801564.
(29) Li, W.; Watzele, S.; El-Sayed, H. A.; Liang, Y.; Kieslich, G.; Bandarenka, A. S.; Rodewald, K.; Rieger, B.; Fischer, R. A. Unprecedented High Oxygen Evolution Activity of Electrocatalysts Derived from Surface-Mounted Metal-Organic Frameworks. *J. Am. Chem. Soc.* **2019**, *141*, 5926−5933.
(30) Hai, G.; Jia, X.; Zhang, K.; Liu, X.; Wu, Z.; Wang, G. High-performance oxygen evolution catalyst using two-dimensional ultra-thin metal-organic frameworks nanosheets. *Nano Energy* **2018**, *44*, 345−352.
(31) Liu, B.; Wang, Y.; Peng, H. Q.; Yang, R.; Jiang, Z.; Zhou, X.; Lee, C. S.; Zhao, H.; Zhang, W. Iron Vacancies Induced Bifunctionality in Ultrathin Feroxyhyte Nanosheets for Overall Water Splitting. *Adv. Mater.* **2018**, *30*, 1803144.
(32) Hou, Y.; Hu, W.; Zhou, X.; Gui, Z.; Hu, Y. Vertically Aligned Nickel 2-Methylimidazole Metal−Organic Framework Fabricated from Graphene Oxides for Enhancing Fire Safety of Polystyrene. *Ind. Eng. Chem. Res.* **2017**, *56*, 8778−8786.
(33) Sun, Y.; Pan, J.; Wan, P.; Liu, X. Study on preparation of NiOOH by a new catalytic electrolysis method. *Mater. Res. Bull.* **2009**, *44*, 943−946.
(34) Hu, T.; Wang, Y.; Xiao, H.; Chen, W.; Zhao, M.; Jia, J. Shape-control of super-branched Pd−Cu alloys with enhanced electro-catalytic performance for ethylene glycol oxidation. *Chem. Commun.* **2018**, *54*, 13363−13366.
(35) Ferraro, J. R.; Cristallini, C.; Fox, I. Spectral studies of the rare earth complexes of the type $M(NO_3)_3 \cdot 3TBP$. *J. Inorg. Nucl. Chem.* **1967**, *29*, 139−148.
(36) Zhao, Y.; Yang, X.; Zhan, L.; Ou, S.; Tian, J. High electrocatalytic activity of PtRu nanoparticles supported on starch-functionalized multi-walled carbon nanotubes for ethanol oxidation. *J. Mater. Chem.* **2011**, *21*, 4257−4263.
(37) Zhao, Y.; Yang, X.; Tian, J.; Wang, F.; Zhan, L. A facile and novel approach toward synthetic polypyrrole oligomers functionalization of multi-walled carbon nanotubes as PtRu catalyst support for methanol electro-oxidation. *J. Power Sources* **2010**, *195*, 4634−4640.
(38) Yang, X.; Liu, X.; Meng, X.; Wang, X.; Li, G.; Shu, C.; Jiang, L.; Wang, C. Self-assembly of highly dispersed Pt and PtRu nanoparticles on perylene diimide derivatives functionalized carbon nanotubes as enhanced catalysts for methanol electro-oxidation. *J. Power Sources* **2013**, *240*, 536−543.
(39) Chen, X.; Long, C.; Lin, C.; Wei, T.; Yan, J.; Jiang, L.; Fan, Z. Al and Co co-doped α-$Ni(OH)_2$/graphene hybrid materials with high electrochemical performances for supercapacitors. *Electrochim. Acta* **2014**, *137*, 352−358.
(40) Takahashi, Y.; Kumatani, A.; Munakata, H.; Inomata, H.; Ito, K.; Ino, K.; Shiku, H.; Unwin, P. R.; Korchev, Y. E.; Kanamura, K.; Matsue, T. Nanoscale visualization of redox activity at lithium-ion battery cathodes. *Nat. Commun.* **2014**, *5*, 5450.
(41) Han, M. H.; Gonzalo, E.; Singh, G.; Rojo, T. A comprehensive review of sodium layered oxides: powerful cathodes for Na-ion batteries. *Energy Environ. Sci.* **2015**, *8*, 81−102.
(42) Sasidharan, M.; Senthil, C.; Kumari, V.; Bhaumik, A. The dual role of micelles as templates and reducing agents for the fabrication of catalytically active hollow silver nanospheres. *Chem. Commun.* **2015**, *51*, 733−736.
(43) Yang, X.; Wang, X.; Feng, Y.; Zhang, G.; Wang, T.; Song, W.; Shu, C.; Jiang, L.; Wang, C. Removal of multifold heavy metal contaminations in drinking water by porous magnetic Fe_2O_3@AlO(OH) superstructure. *J. Mater. Chem. A* **2013**, *1*, 473−477.
(44) Aider, N.; Touahra, F.; Bali, F.; Djebarri, B.; Lerari, D.; Bachari, K.; Halliche, D. Improvement of catalytic stability and carbon resistance in the process of CO_2 reforming of methane by CoAl and CoFe hydrotalcite-derived catalysts. *Int. J. Hydrogen Energy* **2018**, *43*, 8256−8266.
(45) Wu, C.; Zhang, J.; Guo, J.; Sun, L.; Ming, J.; Dong, H.; Zhao, Y.; Tian, J.; Yang, X. Ceria-Induced Strategy To Tailor Pt Atomic Clusters on Cobalt−Nickel Oxide and the Synergetic Effect for Superior Hydrogen Generation. *ACS Sustainable Chem. Eng.* **2018**, *6*, 7451−7457.
(46) Zhang, Q.; Yan, D.; Nie, Z.; Qiu, X.; Wang, S.; Yuan, J.; Su, D.; Wang, G.; Wu, Z. Iron-Doped NiCoP Porous Nanosheet Arrays as a Highly Efficient Electrocatalyst for Oxygen Evolution Reaction. *ACS Appl. Energy Mater.* **2018**, *1*, 571−579.
(47) Zhou, D.; Wang, S.; Jia, Y.; Xiong, X.; Yang, H.; Liu, S.; Tang, J.; Zhang, J.; Liu, D.; Zheng, L.; Kuang, Y.; Sun, X.; Liu, B. NiFe Hydroxide Lattice Tensile Strain: Enhancement of Adsorption of Oxygenated Intermediates for Efficient Water Oxidation Catalysis. *Angew. Chem., Int. Ed.* **2019**, *58*, 736−740.
(48) Wu, C.; Guo, J.; Zhang, J.; Zhao, Y.; Tian, J.; Isimjan, T. T.; Yang, X. Palladium nanoclusters decorated partially decomposed porous ZIF-67 polyhedron with ultrahigh catalytic activity and stability on hydrogen generation. *Renewable Energy* **2019**, *136*, 1064−1070.
(49) Gan, Q.; Cheng, X.; Chen, J.; Wang, D.; Wang, B.; Tian, J.; Isimjan, T. T.; Yang, X. Temperature effect on crystallinity and chemical states of nickel hydroxide as alternative superior catalyst for urea electrooxidation. *Electrochim. Acta* **2019**, *301*, 47−54.
(50) Li, Q.; Pan, H.; Higgins, D.; Cao, R.; Zhang, G.; Lv, H.; Wu, K.; Cho, J.; Wu, G. Metal−Organic Framework-Derived Bamboo-like Nitrogen-Doped Graphene Tubes as an Active Matrix for Hybrid Oxygen-Reduction Electrocatalysts. *Small* **2015**, *11*, 1443−1452.
(51) Cheng, X.; Yan, P.; Liu, S.; Qian, M.; Wang, B.; Wan, Z.; Tian, J.; Shen, X.-C.; Isimjan, T. T.; Yang, X. Well-dispersed iron oxide stabilized Fe N_4 active sites in porous N-doped carbon spheres as alternative superior catalyst for oxygen reduction. *Int. J. Hydrogen Energy* **2019**, *44*, 12127−12137.
(52) Xing, J.; Guo, K.; Zou, Z.; Cai, M.; Du, J.; Xu, C. In situ growth of well-ordered NiFe-MOF-74 on Ni foam by Fe^{2+} induction as an efficient and stable electrocatalyst for water oxidation. *Chem. Commun.* **2018**, *54*, 7046−7049.
(53) Duan, J.; Chen, S.; Zhao, C. Ultrathin metal-organic framework array for efficient electrocatalytic water splitting. *Nat. Commun.* **2017**, *8*, 15341.
(54) Zhu, R.; Ding, J.; Xu, Y.; Yang, J.; Xu, Q.; Pang, H. π-Conjugated Molecule Boosts Metal−Organic Frameworks as Efficient Oxygen Evolution Reaction Catalysts. *Small* **2018**, *14*, 1803576.
(55) Jayaramulu, K.; Masa, J.; Morales, D. M.; Tomanec, O.; Ranc, V.; Petr, M.; Wilde, P.; Chen, Y.-T.; Zboril, R.; Schuhmann, W.; Fischer, R. A. Ultrathin 2D Cobalt Zeolite-Imidazole Framework Nanosheets for Electrocatalytic Oxygen Evolution. *Adv. Sci.* **2018**, *5*, 1801029.
(56) Zhu, X.; Tang, C.; Wang, H.-F.; Li, B.-Q.; Zhang, Q.; Li, C.; Yang, C.; Wei, F. Monolithic-structured ternary hydroxides as freestanding bifunctional electrocatalysts for overall water splitting. *J. Mater. Chem. A* **2016**, *4*, 7245−7250.
(57) Ou, G.; Fan, P.; Zhang, H.; Huang, K.; Yang, C.; Yu, W.; Wei, H.; Zhong, M.; Wu, H.; Li, Y. Large-scale hierarchical oxide nanostructures for high-performance electrocatalytic water splitting. *Nano Energy* **2017**, *35*, 207−214.
(58) Li, W.; Gao, X.; Xiong, D.; Wei, F.; Song, W.-G.; Xu, J.; Liu, L. Hydrothermal Synthesis of Monolithic Co_3Se_4 Nanowire Electrodes for Oxygen Evolution and Overall Water Splitting with High Efficiency and Extraordinary Catalytic Stability. *Adv. Energy Mater.* **2017**, *7*, 1602579.
(59) Meng, H.; Ren, Z.; Du, S.; Wu, J.; Yang, X.; Xue, Y.; Fu, H. Engineering a stereo-film of $FeNi_3$ nanosheet-covered FeOOH arrays for efficient oxygen evolution. *Nanoscale* **2018**, *10*, 10971−10978.
(60) Luo, J.; Im, J.-H.; Mayer, M. T.; Schreier, M.; Nazeeruddin, M. K.; Park, N.-G.; Tilley, S. D.; Fan, H. J.; Grätzel, M. Water photolysis at 12.3% efficiency via perovskite photovoltaics and Earth-abundant catalysts. *Science* **2014**, *345*, 1593−1596.
(61) Yang, Y.; Fei, H.; Ruan, G.; Xiang, C.; Tour, J. M. Efficient Electrocatalytic Oxygen Evolution on Amorphous Nickel−Cobalt Binary Oxide Nanoporous Layers. *ACS Nano* **2014**, *8*, 9518−9523.
(62) Gorlin, M.; Chernev, P.; Ferreira de Araujo, J.; Reier, T.; Dresp, S.; Paul, B.; Krahnert, R.; Dau, H.; Strasser, P. Oxygen Evolution

DOI: 10.1021/acsanm.9b01330
ACS Appl. Nano Mater. 2019, 2, 6334−6342

Reaction Dynamics, Faradaic Charge Efficiency, and the Active Metal Redox States of Ni-Fe Oxide Water Splitting Electrocatalysts. *J. Am. Chem. Soc.* **2016**, *138*, 5603−5614.
(63) Li, N.; Bediako, D. K.; Hadt, R. G.; Hayes, D.; Kempa, T. J.; von Cube, F.; Bell, D. C.; Chen, L. X.; Nocera, D. G. Influence of iron doping on tetravalent nickel content in catalytic oxygen evolving films. *Proc. Natl. Acad. Sci. U. S. A.* **2017**, *114*, 1486−1491.
(64) Guo, J.; Sun, J.; Sun, Y.; Liu, Q.; Zhang, X. Electrodepositing Pd on NiFe layered double hydroxide for improved water electrolysis. *Mater. Chem. Front.* **2019**, *3*, 842−850.
(65) Li, Y.; Lu, M.; Wu, Y.; Xu, H.; Gao, J.; Yao, J. Trimetallic Metal−Organic Framework Derived Carbon-Based Nanoflower Electrocatalysts for Efficient Overall Water Splitting. *Adv. Mater. Interfaces* **2019**, *6*, 1900290.
(66) Luo, Y.; Tang, L.; Khan, U.; Yu, Q.; Cheng, H. M.; Zou, X.; Liu, B. Morphology and surface chemistry engineering toward pH-universal catalysts for hydrogen evolution at high current density. *Nat. Commun.* **2019**, *10*, 269.

DOI: 10.1021/acsanm.9b01330
ACS Appl. Nano Mater. 2019, 2, 6334−6342